ACS OMEGA

Open Access

This article is licensed under CC-BY-NC-ND 4.0

http://pubs.acs.org/journal/acsodf

Article

Multimodal Molecular Imaging Reveals a Novel Membrane Component in Sporangia of the Rare Actinomycete *Actinoplanes missouriensis*

Keisuke Usami, Takeaki Tezuka, Yasuo Ohnishi, and Shinsuke Shigeto*

Cite This: *ACS Omega* 2024, 9, 39956−39964

Read Online

ACCESS | Metrics & More | Article Recommendations | Supporting Information

ABSTRACT: The bacterium *Actinoplanes missouriensis* belongs to the genus *Actinoplanes*, a prolific source of useful natural products. This microbe forms globular structures called sporangia, which contain many dormant spores. Recent studies using transmission electron microscopy have shown that the *A. missouriensis* sporangium membrane has an unprecedented three-layer structure, but its molecular components remain unclear. Here, we present multimodal (spontaneous Raman scattering, coherent anti-Stokes Raman scattering, second harmonic generation, sum frequency generation, and third-order sum frequency generation) label-free molecular imaging of intact *A. missouriensis* sporangia. Spontaneous Raman imaging assisted with multivariate curve resolution−alternating least-squares analysis revealed a novel component in the sporangium membrane that exhibits unique Raman bands at 1550 and 1615 cm^{-1} in addition to those characteristic of lipids. A plausible candidate for this component is an unsaturated carbonyl compound with an aliphatic moiety derived from fatty acid. Furthermore, second harmonic generation imaging revealed that a layer(s) of the sporangium membrane containing this unknown component has an ordered, noncentrosymmetric structure like fibrillar proteins and amylopectin. Our results suggest that the sporangium membrane is a new type of biological membrane, not only in terms of architecture but also in terms of components. We demonstrate that multimodal molecular imaging with Raman scattering as the core technology will provide a promising platform for interrogating the chemical components, whether known or unknown, of diverse biological structures produced by microbes.

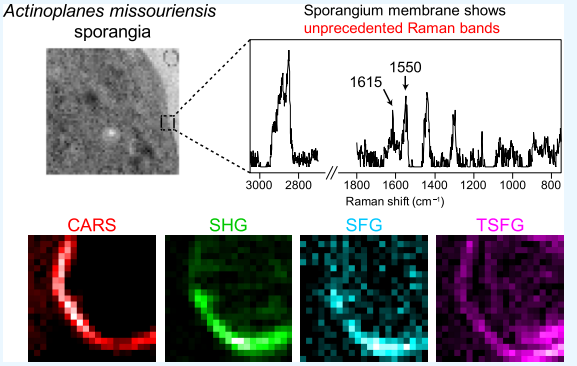

INTRODUCTION

Membranes and walls are essential elements for almost all microbes, defining the boundary between the organism and the environment.[1] They are constructed from lipid bilayers as their fundamental building blocks, but their architecture and components vary widely. For instance, Gram-positive bacteria have a thick layer of peptidoglycan in their cell wall, whereas Gram-negative bacteria have an outer membrane in addition to a thin layer of peptidoglycan. Archaea have membrane structures that are distinctly different from those of bacteria. The archaeal membrane typically consists of lipids composed of glycerol and isoprenoid alcohols linked by an ether linkage, instead of those composed of glycerol and fatty acids linked by an ester linkage found in the bacterial membrane.[2,3] In addition, the outer surface of almost all archaea and many bacteria is coated with a paracrystalline proteinaceous layer known as an S-layer.[4] Although our understanding of microbial membranes and walls has greatly advanced, the vast majority of microbes are still unknown due to the limitations of conventional culture methods,[5] so novel membrane structures and components likely remain to be discovered.

Recently, such a discovery has been made in studies of the soil-dwelling bacterium *Actinoplanes missouriensis*. The genus *Actinoplanes* is a rich source of natural products, including enzymes and antibiotics,[6−8] of which *A. missouriensis* is a representative species.[9,10] *A. missouriensis* is classified as a rare actinomycete because of its apparently low isolation frequency compared to the dominant genus *Streptomyces*. This microbe exhibits a complex morphological development: it grows substrate mycelia during vegetative growth and forms globose or subglobose structures at the end of the mycelia, known as sporangia. Each sporangium contains a few hundred dormant sporangiospores and can be thought of as a multicellular organ in prokaryotes. Sporangium formation and dehiscence have received much attention to elucidate the complex morphological development in *A. missouriensis*.[11−13] Interestingly,

Received: June 19, 2024
Revised: August 23, 2024
Accepted: August 28, 2024
Published: September 9, 2024

© 2024 The Authors. Published by American Chemical Society

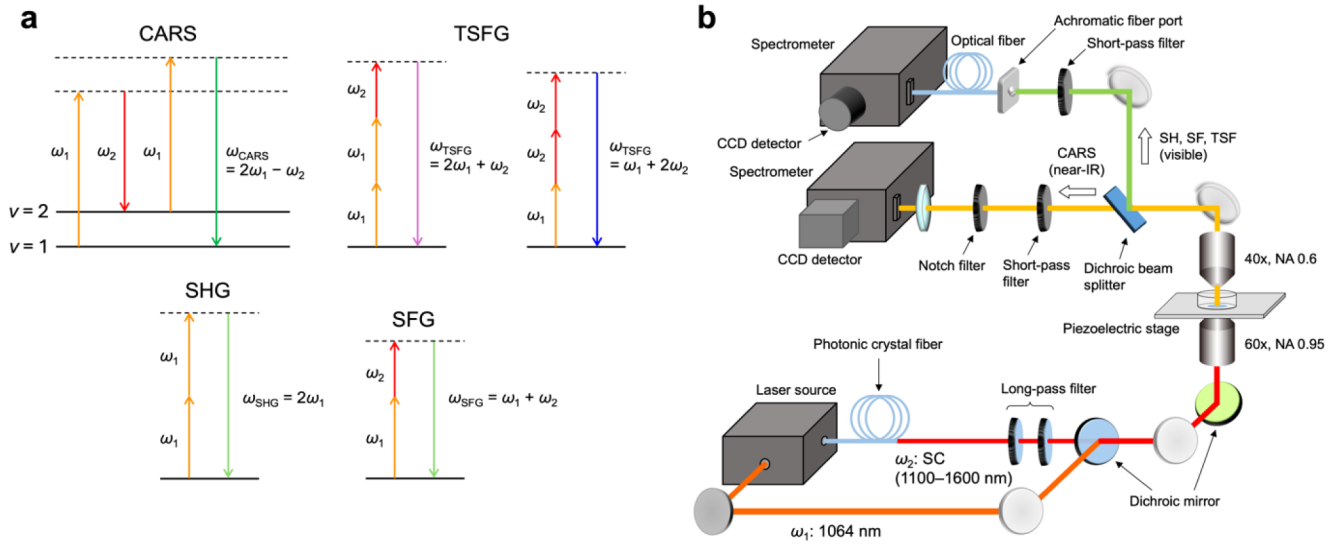

Figure 1. (a) Energy diagrams of the nonlinear optical processes observed in this study: CARS, TSFG, SHG, and SFG. CARS and TSFG are third-order nonlinear optical processes, and SHG and SFG are second-order nonlinear optical processes. (b) Schematic diagram of the multimodal (CARS/SHG/SFG/TSFG) nonlinear optical imaging setup developed in this study.

recent studies using transmission electron microscopy (TEM) and atomic force microscopy have shown that the sporangium membrane is composed of three layers of different thicknesses.[14,15] It is also known empirically that the outermost layer of the sporangia (i.e., the sporangium surface) is hydrophobic. These observations suggest that the sporangium membrane may be a novel type of microbial membrane (or wall). However, little is known about its components due to the lack of chemical specificity of the above-mentioned techniques.

In this work, we used multimodal, label-free molecular imaging to detect and visualize the components of intact *A. missouriensis* sporangia. Label-free molecular imaging has emerged as an effective tool for visualizing a biological sample, such as living cells and tissues, without the need for an exogenous label and without disrupting the integrity of the sample. The multimodality we achieved here includes spontaneous Raman scattering and nonlinear optical processes[16−18] such as coherent anti-Stokes Raman scattering (CARS), second harmonic generation (SHG), sum frequency generation (SFG), and third-order sum frequency generation (TSFG). The energy diagrams of these processes are depicted in Figure 1a. Spontaneous Raman scattering, which probes vibrational transitions, provides otherwise unobtainable information about molecular identity, structure, and interactions. CARS is a third-order nonlinear variant of spontaneous Raman scattering. Although the vibrational information contained in a CARS spectrum, if properly extracted (see below), is essentially the same as that of the corresponding spontaneous Raman spectrum, CARS has the advantage of higher signal intensities than spontaneous Raman scattering due to coherent signal generation. This advantage makes CARS particularly suitable for high-speed imaging.[19,20] SHG is a second-order nonlinear optical process that occurs at twice the angular frequency and half the wavelength of the incident light. It arises exclusively from media lacking a center of symmetry (e.g., surfaces and interfaces, fibrillar proteins such as collagen and myosin, and starch).[21−23] SFG is similar in mechanism to SHG, except that it involves the mixing of two photons of different energies. The third-order nonlinear optical process TSFG is an analog of third harmonic generation[24−26] (THG), which has been widely used as a versatile method for bioimaging. Like THG, TSFG is expected to occur at structural interfaces where there is a change in optical properties such as refractive index.

We capitalized on multiple contrast enhancements resulting from the different mechanisms of these optical processes. Raman imaging (both spontaneous Raman and CARS) with the help of multivariate curve resolution−alternating least-squares (MCR−ALS) analysis revealed an as-yet-unknown component that is localized to the sporangium membrane. We found that this component not only has many of the Raman features of lipids but is also characterized by two unique bands that have not been observed in typical biological molecules. Furthermore, SHG imaging showed that the sporangium membrane containing this novel molecular species has an ordered, noncentrosymmetric structure.

EXPERIMENTAL SECTION

Sample Preparation. *A. missouriensis* sporangia were prepared according to the literature.[11,27] *A. missouriensis* 431^T (NBRC 102363^T) was grown on YBNM agar medium (0.1% yeast extract, 0.07% bonito extract, 0.2% NZ amine, 1% maltose monohydrate, and 2% agar; pH 7.0) at 30 °C for more than 2 days. A 1 cm × 1 cm piece of the YBNM agar on which *A. missouriensis* mycelia were grown was cut and placed in PYM liquid medium (0.5% peptone, 0.3% yeast extract, and 0.1% $MgSO_4{\cdot}7H_2O$; pH 7.0), followed by shaking incubation at 120 rpm at 30 °C for 2 days. After being collected from the liquid medium by centrifugation at 3500 rpm at room temperature for 10 min, the cells were suspended in 0.75% NaCl solution. The suspension was again centrifuged at 3500 rpm at room temperature for 10 min. The sedimented cells were resuspended in 0.75% NaCl solution. A 100 μL portion of the cell suspension was inoculated on humic acid-trace element (HAT) agar medium (0.1% sucrose, 0.01% Casamino acids, 0.05% K_2HPO_4, 0.5% nitrohumic acid solution, 1% trace element solution, and 2% agar; pH 7.5). The nitrohumic acid solution was prepared by slowly adding 100 mL of 0.8% NaOH solution to 10 g of nitrohumic acid powder. The trace

https://doi.org/10.1021/acsomega.4c05706
ACS Omega 2024, 9, 39956−39964

element solution contained 0.004% $ZnCl_2$, 0.02% $FeCl_3 \cdot 6H_2O$, 0.001% $CuCl_2 \cdot 2H_2O$, 0.001% $MnCl_2 \cdot 4H_2O$, 0.001% $Na_2B_4O_7 \cdot 10H_2O$, and 0.001% $(NH_4)_6Mo_7O_{24} \cdot 4H_2O$. The HAT agar plate was incubated at 30 °C for more than 7 days to form sporangia on substrate mycelia. Prior to use for imaging experiments, the sporangia formed on the HAT agar plate were harvested using an inoculation loop and suspended in 300 μL of 50 mM NaCl solution, in which sporangium dehiscence was not induced. A 100 μL portion of the suspension was transferred to a glass bottom dish and used as the sample for imaging experiments.

Spontaneous Raman Imaging. Space-resolved spontaneous Raman spectra covering both the C−H stretching and fingerprint regions were measured using a laboratory-built confocal Raman microspectrometer based on a customized Nikon inverted microscope (TE2000-U), which has been described previously.[28,29] Briefly, a 632.8 nm He−Ne laser was used as the excitation light source. The laser beam was focused onto the sample placed on a piezoelectric stage with an oil-immersion objective (100×, NA = 1.45; CFI Plan Apo Lambda, Nikon), and backscattered light was collected with the same objective. The laser power at the sample was 7 mW. The sample was raster-scanned with the piezoelectric stage at 0.3 μm intervals. Only the Stokes Raman component of the backscattered light was wavelength-dispersed with an imaging spectrometer and detected with an electron-multiplying charge-coupled device (CCD) camera. The CCD exposure time was set to 1 s/pixel. The spatial resolution of the apparatus was estimated to be 0.43 μm in the lateral direction and 4.4 μm in the axial direction.

Multimodal Nonlinear Optical Imaging. In this study, we have developed a multimodal nonlinear optical imaging system (see Figure 1b for its schematic illustration) based on the broadband multiplex CARS microspectrometer that we reported previously.[30] We have extended the apparatus to be able to detect the visible signals originating from nonlinear optical processes such as SHG, SFG, and TSFG that occur simultaneously with the near-IR CARS. The multiplex CARS part is the same as that described in our recent paper.[30] A broadband supercontinuum (SC) light source (OPERA, Leukos) using a subnanosecond microchip laser[31] operating at ∼30 kHz as the master laser source and a photonic crystal fiber generates both narrowband 1064 nm and broadband SC beams. The former was used as the pump (ω_1) beam, and the near-IR portion of the latter as the Stokes (ω_2) beam for multiplex CARS. The broadband ω_2 spectrum covered 1100−1600 nm, corresponding to Raman shifts of 300−3150 cm^{-1}. The collinearly overlapped ω_1 and ω_2 beams were focused onto the sample mounted on a piezoelectric stage (Nano-LP300, Mad City Laboratories) with a dry objective (60×, NA = 0.95; CFI Plan Apo Lambda, Nikon). The average powers of the ω_1 and ω_2 beams were 10.0 mW and 1.75 mW for CARS imaging only and 16.0 mW and 1.85 mW for CARS/SHG/SFG/TSFG imaging, respectively. The ω_1 and ω_2 beams were both linearly polarized and set parallel to each other. The forward-propagating signal was collected with a dry objective (40×, NA = 0.60; CFI Plan Fluor ELWD, Nikon) and split into the visible and near-IR by a dichroic beam splitter (FF735-Di02-25×36, Semrock). As in the spontaneous Raman imaging described above, the sample was translated in a raster manner with a 0.3 μm step using the piezoelectric stage. The near-IR part, which contains CARS signals at $\omega_{CARS} = 2\omega_1 - \omega_2$, was analyzed with a spectrograph (Acton SP-2358, Teledyne Princeton Instrument) and detected with a high-speed CCD camera (BLAZE 100-HRX, Teledyne Princeton Instruments), as described previously.[30] The visible part, which contains SHG ($\omega_{SHG} = 2\omega_1$), SFG ($\omega_{SFG} = \omega_1 + \omega_2$), and TSFG ($\omega_{TSFG} = 2\omega_1 + \omega_2$ and $\omega_1 + 2\omega_2$) signals, was passed through a short-pass filter (BSP01−785R-25, Semrock) to eliminate the incident ω_1 and ω_2 beams. Subsequently, the signal light was introduced into an optical fiber (M92L01, Thorlabs) using an achromatic fiber port (PAF2S-A4A, Thorlabs), analyzed with a spectrograph (HRS-300, Teledyne Princeton Instruments), and detected with a CCD camera (PIXIS 100BR eXcelon, Teledyne Princeton Instruments). Because the two CCD cameras and the piezoelectric stage were electrically synchronized, the near-IR (CARS) and visible (SHG, SFG, and TSFG) spectra could be acquired simultaneously. The CCD exposure time was set to 0.1 s/pixel for CARS imaging only and 0.8 s/pixel for CARS/SHG/SFG/TSFG imaging. The spatial resolution of the apparatus for CARS was estimated to be 0.44 μm in the lateral direction and 3.4 μm in the axial direction.

Spectral Analysis. *Spontaneous Raman Spectra.* First, the spectrum of the 50 mM NaCl solution measured separately was subtracted from all Raman spectra of the sporangium sample. The background-subtracted spectra were subjected to an intensity correction using a calibrated halogen light source (Ocean Insight, HL-3P-CAL). Next, noise reduction was performed with singular value decomposition (SVD).[32,33] Singular components up to 13 were retained as meaningful components. Asymmetrically reweighted penalized least-squares smoothing[34] (arPLS) was employed to correct the baseline arising primarily from autofluorescence. The smoothness parameter in arPLS, λ, which needs to be adjusted depending on the noise level of the data, was set to 10^6. Finally, the preprocessed hyperspectral Raman imaging data were analyzed using MCR−ALS, a multivariate data analysis technique.

MCR−ALS assumes that a hyperspectral imaging matrix **A** can be expressed as a linear combination of several major chemical components. Under this assumption, MCR−ALS searches for the optimal decomposition of **A** into the product of matrices **W** and **H**:

$$\mathbf{A} \approx \mathbf{WH} \tag{1}$$

where all elements of **W** and **H** are restricted to be non-negative.[35,36] In the present case, **A** is an $m \times n$ matrix, where m is the number of CCD pixels and n is the number of the Raman spectra (i.e., the number of measurement points). The columns of the $m \times k$ matrix **W** represent the intrinsic Raman spectrum of each component, and the rows of the $k \times n$ matrix **H** represent its spatial concentration profile (i.e., the Raman image). k is the number of the underlying components and must be inferred, e.g., by reference to the magnitudes of singular values and/or *a priori* knowledge of the sample. In this study, the value of k that yields the most reasonable decomposition was found to be 4 (see below for more details). Unlike principal component analysis and SVD, eq 1 is not a unique decomposition, so it must be iteratively solved via ALS[35] so that the Frobenius norm $\|\mathbf{A} - \mathbf{WH}\|_F$ is minimized. Initial guesses for **W** and **H** were generated from the SVD results.[37] L1 regularization (also known as Lasso[38]) was applied to obtain sparser solutions by adding the absolute value of each element of the solution, $\Lambda\Sigma_j|\beta_j|$, as a penalty term. The value of Λ was determined on a case-by-case basis, and $\Lambda = 3$

https://doi.org/10.1021/acsomega.4c05706
ACS Omega 2024, 9, 39956−39964

$\times 10^{-5}$ was chosen for the MCR−ALS analysis of the spontaneous Raman imaging results. A more detailed description of MCR−ALS can be found in our previous paper.[32]

Multiplex CARS Spectra. Unlike spontaneous Raman spectra, as-measured CARS spectra do not represent true vibrational spectra due to interference with the nonresonant background that always accompanies vibrationally resonant signals. This interference leads to typical dispersive spectral patterns, which can very often hamper accurate interpretation and quantitative analysis, such as SVD and MCR−ALS. It is therefore necessary to extract the vibrationally resonant component, namely, the imaginary part of the third-order nonlinear susceptibility, $\mathrm{Im}[\chi^{(3)}]$. In this study, the $\mathrm{Im}[\chi^{(3)}]$ spectra were retrieved from raw CARS spectra using the maximum entropy method[39,40] (MEM). CARS spectra measured in a sporangium were first divided by the spectrum of the NaCl solution measured on the same focal plane in the same sample, which served as the nonresonant background. The $\mathrm{Im}[\chi^{(3)}]$ spectra, equivalent to spontaneous Raman spectra, were then deduced by estimating the phase function from the profile obtained by arPLS baseline correction ($\lambda = 10^6$). The retrieved $\mathrm{Im}[\chi^{(3)}]$ spectra were then denoised with SVD (10 singular components retained) and analyzed with MCR−ALS, in which $k = 4$ was assumed and an L1 penalty with $\Lambda = 1 \times 10^{-3}$ was imposed.

The SVD noise reduction was performed on Igor Pro 9 (WaveMetrics), while the arPLS, MEM, and MCR−ALS calculations were performed using Python code written in-house.

RESULTS AND DISCUSSION

MCR−ALS Spontaneous Raman Imaging. First, we performed spontaneous Raman imaging of a single *A. missouriensis* sporangium (see the bright-field image in Figure 2a) in 50 mM NaCl solution harvested from the surface of HAT agar,[11,27] using the laboratory-built, 632.8 nm-excited confocal Raman microspectrometer.[28,29] The obtained hyperspectral Raman imaging data were dominated by the Raman signals of spores in the sporangium and an intrasporangial matrix (see below), making it difficult to discern those of minor components. Therefore, we applied MCR−ALS[30,32,41] to elicit the spectral and spatial information on such elusive components. We have previously demonstrated the utility of MCR−ALS in molecular imaging of microbes such as a fission yeast,[32] a filamentous fungus,[41] and a thraustochytrid.[30] Owing to non-negativity constraints,[35,36] MCR−ALS facilitates decomposing hyperspectral Raman imaging data into directly interpretable components. In the present MCR−ALS analysis, we assumed four components ($k = 4$), one of which represents nothing but the remainder of the background correction that was present outside the sporangium. The MCR−ALS-derived spatial distributions (Raman images) and spectra of the other meaningful components (labeled 1−3) are shown in Figure 2a,b, respectively.

Component 1 shows typical Raman bands assignable to proteins, including the amide I band at 1665 cm^{-1}, the amide III band at 1255 cm^{-1}, and the ring breathing band of the phenylalanine residues at 1003 cm^{-1} (Figure 2b, yellow). More detailed band assignments are given in Table S1. The Raman spectrum of component 2 (Figure 2b, blue) is dominated by three sharp bands at 1512, 1154, and 1003 cm^{-1}, although the protein Raman bands described above also contribute to a lesser extent. The three bands are Raman bands of carotenoids resonantly enhanced by the visible (632.8 nm) excitation: the 1512 cm^{-1} band is assigned to the in-phase C=C stretching mode of the conjugated chain of carotenoids, the 1154 cm^{-1} band to the C−C stretching mode, and the 1003 cm^{-1} band to the $C-CH_3$ rocking mode.[42] The Raman spectra of components 1 and 2 are well-known in Raman spectroscopy of biological samples, and indeed, numerous papers have reported similar spectra. The molecular compositions of the spores and sporangium matrix have not yet been fully elucidated, but from their spatial distributions (Figure 2a, yellow and blue), components 1 and 2 can be attributed primarily to the sporangium matrix and spores, respectively. The presence of carotenoids in spores (more specifically, in the spore membrane) appears to be consistent with the yellowish color of spores released from sporangia (i.e., zoospores).[27] *A. missouriensis* has been shown to produce phleixanthophyll (unpublished result).

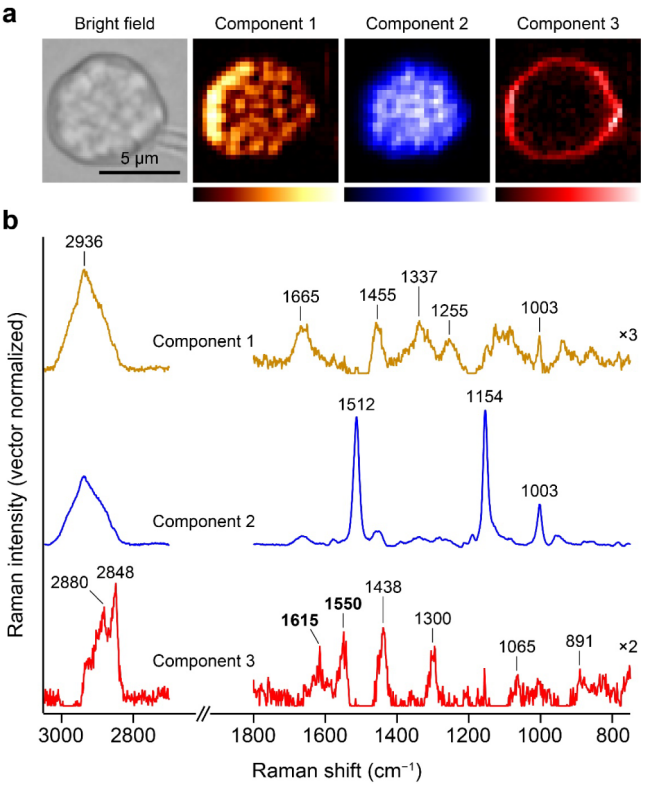

Figure 2. MCR−ALS results of spontaneous Raman imaging of an *A. missouriensis* sporangium in 50 mM NaCl solution. (a) Bright-field image of the sporangium and Raman images presented in pseudocolor of components 1−3. (b) Raman spectra of components 1−3. In the MCR−ALS analysis, four components were assumed, but one of them represents only a residual background, so it is omitted here. The spectra have been vector-normalized and are offset for clarity of display. For better visibility, the fingerprint region (750−1800 cm^{-1}) of the spectra of components 1 and 3 have been multiplied by a factor of 3 and 2, respectively. Scale bar = 5 μm.

Component 3 is localized at the periphery of the sporangium (Figure 2a, red) and is therefore unequivocally attributed to a major component of the sporangium membrane. We have, for the first time to our knowledge, visualized the membrane of an intact *A. missouriensis* sporangium using spontaneous Raman imaging. In contrast to components 1 and 2, the Raman spectrum of component 3 (Figure 2b, red) is rather unusual; it

https://doi.org/10.1021/acsomega.4c05706
ACS Omega 2024, 9, 39956−39964

exhibits two prominent bands at 1550 and 1615 cm^{-1}, besides other familiar bands, e.g., at 1300 and 1438 cm^{-1}. We confirmed that similar MCR−ALS results were obtained from other sporangia.

We also attempted MCR−ALS analysis with other numbers of components, but the results were not as physically and biologically sound as that with $k = 4$. For example, $k = 3$ failed to extract a component localized to the sporangium membrane, and $k = 5$ resulted in many problems, including the appearance of multiple background components and dips at some band positions, and imperfect separation of the carotenoid component.

Because the decomposition by MCR−ALS is not unique, one might suspect that the spectral features at 1550 and 1615 cm^{-1} of component 3 could be some kind of artifact caused by the analysis. However, this is not the case. Knowing the exact locations (i.e., pixels) of the sporangium membrane and the inner part of the sporangium from the MCR−ALS Raman images of components 2 and 3, we were able to calculate the averaged spectrum of the sporangium membrane directly from the original hyperspectral imaging data. As compared in Figure 3, the averaged spectrum of the sporangium membrane so

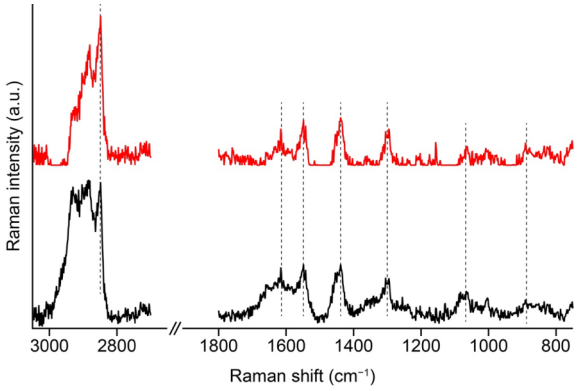

Figure 3. Comparison of the Raman spectra of the sporangium membrane derived from the MCR−ALS analysis (red line, same as in Figure 2b) and calculated directly from the preprocessed spectra without resorting to MCR−ALS (black line). The black spectrum was obtained by appropriately subtracting the spectrum calculated by averaging all spectra at positions with intensities greater than 50% of the maximum of the MCR−ALS Raman image of component 2 (Figure 2a, blue) from that of component 3 (Figure 2a, red) calculated in the same manner as above. These spectra are shown in Figure S2a,b. The inner spectrum was multiplied by a coefficient such that the carotenoid band at 1154 cm^{-1} disappears after the subtraction. The subtraction of the inner spectrum was necessary; due to the limited spatial resolution of the present experiment, the membrane spectrum is strongly influenced by the exceedingly strong Raman bands of the carotenoids found inside the sporangium. The difference spectrum (Figure S2c) was then subjected to baseline correction, and the resulting spectrum is shown as the black spectrum in this figure. The spectra are offset for clarity of display.

obtained agrees very well with the spectrum of component 3, thus validating the MCR−ALS result. Although the images constructed using the area intensities of Raman bands at, e.g., 1550 and 2848 cm^{-1} (univariate Raman images[32,43]) could visualize the sporangium membrane with somewhat poorer contrast (Figure S1), MCR−ALS surpasses the univariate analysis in that it provides a complete profile of the intrinsic spectrum of the membrane component, facilitating the elucidation of its molecular origin.

Multimodal Nonlinear Optical Imaging. To gain further insight into this unknown component of the sporangium membrane, we next applied multimodal nonlinear optical imaging to *A. missouriensis* sporangia. In this study, we have extended the multiplex CARS microspectrometer[30] that we recently constructed using a near-IR SC light source[31] to simultaneously detect nonlinear optical signals appearing in the visible region, such as SHG, SFG, and TSFG signals. The broad spectral coverage of the ω_2 beam enables us to achieve multiplex CARS,[31,44] by which multiple molecular vibrations are simultaneously detected. Similarly, other processes involving the interaction with the ω_2 beam (i.e., SFG and TSFG) are also multiplexed.

Figure 4a shows a representative visible spectrum measured on the sporangium membrane. We were able to observe three distinct features in the visible region. The sharp band observed at 532 nm is the SHG signal ($\omega_{SHG} = 2\omega_1$). The band at longer wavelengths relative to the SHG band is the multiplex SFG signal ($\omega_{SFG} = \omega_1 + \omega_2$; $\omega_1 > \omega_2$), whose broad bandwidth reflects the SC spectrum of the ω_2 light. The other broad band at shorter wavelengths relative to the SHG band can be assigned to the multiplex TSFG signal ($\omega_{TSFG} = 2\omega_1 + \omega_2$ and $\omega_1 + 2\omega_2$). This assignment is corroborated by the fact that the observed wavelength range (approximately 360−470 nm) is consistent with that predicted from the energy conservation relations $\omega_{TSFG} = 2\omega_1 + \omega_2$ and $\omega_1 + 2\omega_2$. We did not observe noticeable THG signals in the sporangium as opposed to previous studies on budding yeast[18] and nematode cells.[45]

In addition to SHG, SFG, and TSFG, we also observed multiplex CARS signals in the near-IR region ($\omega_{CARS} = 2\omega_1 - \omega_2$; Figure 4b). Plotted in this figure is the imaginary part of the third-order optical susceptibility responsible for CARS, $\mathrm{Im}[\chi^{(3)}]$. It was retrieved from raw CARS spectra distorted as a result of interference with a nonresonant background using MEM,[39,40] as already described in the Experimental Section. The $\mathrm{Im}[\chi^{(3)}]$ spectra are, in principle, equivalent to spontaneous Raman spectra. As in spontaneous Raman imaging, the 1550 cm^{-1} band, which is one of the markers for the unknown component of the sporangium membrane, is clearly seen. The 1615 cm^{-1} band probably overlaps with the amide I band of proteins. Note that the representative CARS spectrum shown in Figure 4b is an original spectrum and not a pure component spectrum derived from MCR−ALS analysis (the spectra shown in Figure 2b). Even with the near-IR excitation, the 1550 cm^{-1} band remained unchanged in terms of relative intensities. This result implies that the unknown component is not resonantly enhanced by the visible excitation. In separate experiments, we also performed MCR−ALS of hyperspectral CARS ($\mathrm{Im}[\chi^{(3)}]$) imaging, and the results (Figure S3) are qualitatively similar to those of spontaneous Raman imaging (Figure 2), except for the absence of carotenoids, as expected, because of the near-IR excitation.

Figure 4c shows the CARS (the 1550 cm^{-1} band), SHG, SFG, and TSFG images represented in pseudocolor, together with the bright-field image of the sporangium. These images were constructed using the area intensities of the corresponding signals. All the images reveal distributions localized to the sporangium membrane. TSFG is thought to be sensitive to interfaces where the refractive index changes significantly.[18] Therefore, it should be observable at the outermost layer of the sporangium membrane, producing an image like the magenta

https://doi.org/10.1021/acsomega.4c05706
ACS Omega 2024, 9, 39956−39964

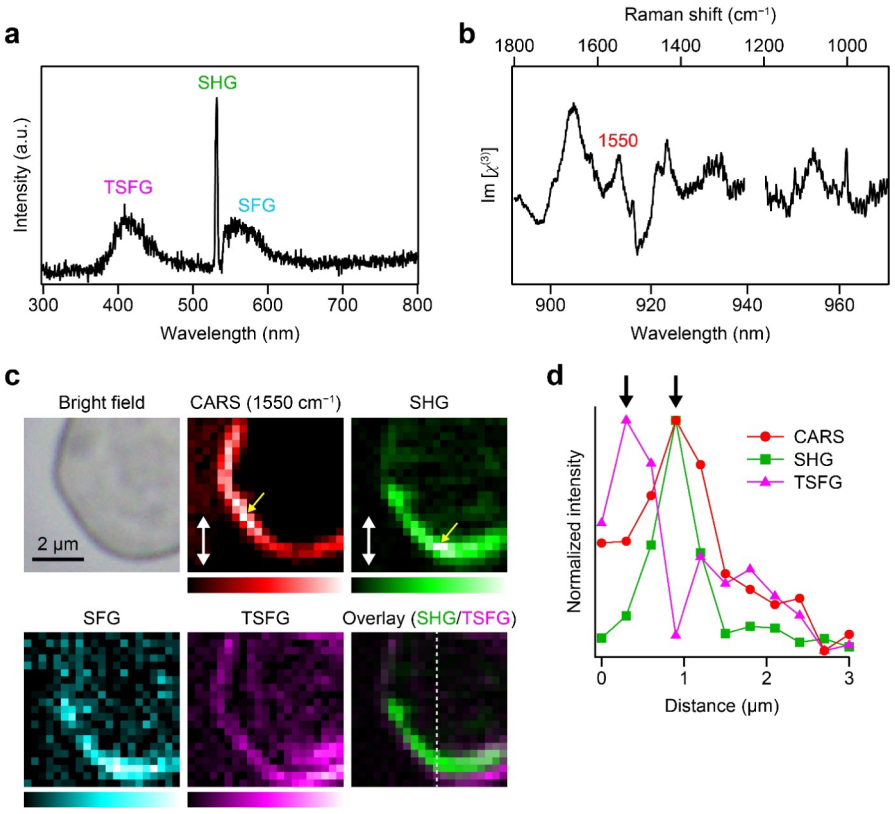

Figure 4. Multimodal nonlinear optical imaging of an *A. missouriensis* sporangium in 50 mM NaCl solution. (a) Representative spectra in the visible region, showing SHG, multiplex SFG, and multiplex TSFG signals. (b) Representative spectra in the near-IR region, showing multiplex CARS signals. The interval between 1200 and 1240 cm^{-1} is not shown due to an unavoidable artifact caused during the spectral analysis. (c) Bright-field image of the sporangium, pseudocolor images of CARS (at 1550 cm^{-1}, red), SHG (green), SFG (cyan), and TSFG (magenta), and an overlaid image of the SHG and TSFG images. The positions where the spectra shown in a,b were measured are indicated by arrows. The excitation polarization direction (both ω_1 and ω_2) is indicated by white double-headed arrows. Scale bar = 2 μm. (d) Line profiles of the CARS (red circles), SHG (green squares), and TSFG (magenta triangles) signals along the dashed line indicated in the overlaid image in c. The profiles are plotted as a function of distance from the outside to the inside of the sporangium membrane. The maxima of the three profiles are indicated by arrows.

one in Figure 4c. In contrast, the clear observation of the SHG and SFG signals from the sporangium membrane was unexpected. This is because SHG from a membrane generally requires a dye to be incorporated into the membrane to break local centrosymmetry. Close examination reveals that the TSFG image is distributed further out in the sporangium membrane compared to the CARS and SHG images. To better see this, we plotted the intensity profiles of the CARS, SHG, and TSFG signals along a line crossing the sporangium membrane (Figure 4d). Although these profiles are considerably broadened due to the spatial resolution of our apparatus (roughly a few hundred nanometers) to give much larger widths than the thickness of the sporangium membrane estimated from previously reported TEM images,[14,15] the CARS and SHG signals become maxima at the same points, whereas the TSFG signal does so ~0.6 μm further out. The spectra at these points are displayed in Figure S4. Taken together, these results suggest that the layer containing the unknown component with the characteristic 1550 and 1615 cm^{-1} bands serves as a harmonophore for SHG (and SFG as well) and corresponds to one or both of the two inner layers (see the Introduction).

It is interesting to note that the regions of the sporangium membrane exhibiting strong signal intensities differ between the CARS and SHG images (Figure 4c): namely, the CARS signal of the 1550 cm^{-1} band is strong in the left part of the image, whereas the SHG signal is strong in the lower part. This observation may be a consequence of the different polarization dependence of CARS and SHG. The polarization of the ω_1 and ω_2 beams is along the direction indicated by the double-headed arrows in the CARS and SHG images in Figure 4c, so the CARS and SHG signals are nearly perpendicular and parallel to the excitation polarization, respectively. Quantitative analysis of the polarization dependence of the SHG signal should provide information on the orientation of the membrane component,[22,46] which is left for future investigation.

Possible Candidate for the Novel Component Found in the Sporangium Membrane. We have presented above our MCR−ALS-assisted spontaneous Raman imaging and tetramodal nonlinear optical imaging results on *A. missouriensis* sporangia and underscored the discovery of the novel SHG-active molecular component in the sporangium membrane. We now ask the most important question: what is this component? Our literature search[47−50] did not come up with any promising candidates. Instead, we found that the Raman spectrum of this novel component (Figure 2b, red) partially resembles that of lipids. In Figure 5, we compare it with the spontaneous Raman spectra of the triacylglycerol (TAG) tripalmitolein and the phospholipids phosphatidylcholine (PC) and phosphatidylserine (PS). As highlighted by gray shading, the spectrum of the sporangium membrane has many Raman bands in common

https://doi.org/10.1021/acsomega.4c05706
ACS Omega 2024, 9, 39956−39964

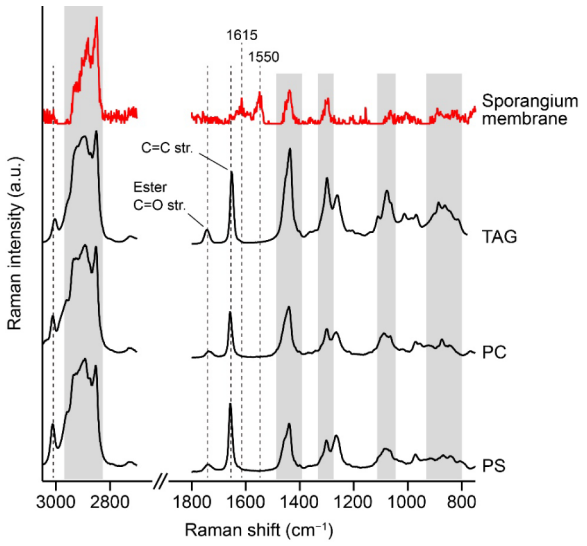

Figure 5. Comparison of the spontaneous Raman spectrum of the sporangium membrane derived from the MCR−ALS analysis (same as in Figure 2b) with those of commercially obtained TAG (tripalmitolein) and phospholipids (PC and PS). Raman bands that are common to all spectra are highlighted by gray shading, and those that are specific to the spectrum of either sporangium membrane or three lipids are indicated by dashed lines. The spectra are offset for clarity of display.

with these lipids. The common bands identified are due to the aliphatic chain (CH_2 and CH_3 groups). On the other hand, there are also notable differences from lipids. Cellular lipids often possess one or more *cis*-C═C bonds, which would manifest as sharp Raman bands at ∼1650 cm^{-1} (*cis*-C═C stretching mode) and ∼3010 cm^{-1} (C−H stretching mode of the C═C−H moiety). In addition, the ester C═O stretching mode would be observed at ∼1740 cm^{-1}. None of these is identified in the spectrum of the unknown component of the sporangium membrane. Based on these similarities and dissimilarities, it is very likely that the component in question is not a lipid (neutral lipid or phospholipid) itself but has a fatty acid-derived moiety.

The accumulated knowledge of vibrational spectroscopy tells us that the spectral window in which the so far unassigned Raman bands at 1550 and 1615 cm^{-1} are found generally contains stretching vibrations associated with double bonds such as C═C, C═O, and C═N. The two characteristic bands of the sporangium membrane could result from a combination of two different types of these double-bond stretching bands. Typically, the C═O stretching frequency is higher than 1700 cm^{-1}, and the C═C and C═N stretching frequencies are between 1600−1680 cm^{-1}. However, these frequencies are highly dependent on the substituent and the environment around the bond (recall an SHG-active ordered structure of the sporangium membrane suggested by our SHG imaging result). This effect may account for the lower-than-expected double-bond frequencies. Given that rare actinomycetes produce diverse carbonyl-containing compounds (i.e., polyketides[51]), an unsaturated carbonyl compound with a fatty acid-derived aliphatic moiety emerges as a likely candidate.

CONCLUSIONS

In the present work, we have successfully visualized the components of sporangia of the rare actinomycete *A. missouriensis* in a nondestructive manner using spontaneous Raman imaging and multimodal (CARS/SHG/SFG/TSFG) nonlinear optical imaging. Most importantly, we have discovered a hitherto unknown component in the sporangium membrane that exhibits Raman bands at ∼1550 and ∼1615 cm^{-1}. Raman imaging is a label-free technique with high molecular specificity, so it has an excellent ability to detect various molecules regardless of their nature (organic/inorganic, polar/nonpolar, small/macromolecules, crystalline/noncrystalline, and so on). This ability can be further enhanced by the use of multivariate data analysis like MCR−ALS employed here. Such versatile detection would be difficult to achieve with other techniques, including fluorescence imaging, which in principle requires fluorescent labeling suitable for (usually known) target molecules. It is this exploratory nature of the Raman spectroscopic approach that led us to the current discovery.

Furthermore, we have found that the sporangium membrane has an SHG-active layer(s). As can be seen from Figure 4c,d, the unknown component revealed by MCR−ALS Raman imaging appears to be present in this SHG-active layer, indicating that the unknown component may form an ordered, noncentrosymmetric structure as in collagen and starch. Previously reported TEM images showed that the *A. missouriensis* sporangium has three layers at the surface,[14,15] but the spatial resolution of our method does not allow us to distinguish between the three layers and to clarify exactly which layer(s) contain the novel component with the SHG-active structure. The middle layer, which was found to be the thickest in the TEM images, is the most conceivable.

We have deduced that the novel component of the sporangium membrane could be a natural product that has an unsaturated carbonyl group and a fatty acid-derived aliphatic chain. The present measurements alone, however, could not fully identify it. Efforts using genetic (e.g., creation of gene-disrupted strains) and biochemical (e.g., extraction of relevant compounds) approaches are currently underway in the laboratory of one of the authors; a putative polyketide synthase is suggested to be involved in the production of a sporangium membrane component. The present findings on the sporangium membrane will not only provide useful guidance for these experiments, but they could also have important implications for the mechanisms of the complex morphological development of *A. missouriensis* because the membrane is the very first site where physical changes in the sporangium take place.

ASSOCIATED CONTENT

Supporting Information

The Supporting Information is available free of charge at https://pubs.acs.org/doi/10.1021/acsomega.4c05706.

Univariate Raman images at 1550 and 2848 cm^{-1} (Figure S1); Raman spectra of the sporangium membrane and the inner part of the sporangium calculated from the original hyperspectral imaging data without using MCR−ALS (Figure S2); MCR−ALS CARS imaging results (Figure S3); visible spectra measured at different positions across the sporangium membrane showing the SHG, SFG, and TSFG signals (Figure S4); and assignments of the major Raman bands observed in *A. missouriensis* sporangia (Table S1) (PDF)

https://doi.org/10.1021/acsomega.4c05706
ACS Omega 2024, 9, 39956−39964

AUTHOR INFORMATION

Corresponding Author

Shinsuke Shigeto − *Department of Chemistry, Graduate School of Science and Technology, Kwansei Gakuin University, Sanda 669-1330, Japan;* orcid.org/0000-0002-2035-2068; Email: shigeto@kwansei.ac.jp

Authors

Keisuke Usami − *Department of Chemistry, Graduate School of Science and Technology, Kwansei Gakuin University, Sanda 669-1330, Japan*

Takeaki Tezuka − *Department of Biotechnology, Graduate School of Agricultural and Life Sciences, The University of Tokyo, Tokyo 113-8657, Japan; Collaborative Research Institute for Innovative Microbiology, The University of Tokyo, Tokyo 113-8657, Japan;* orcid.org/0000-0002-9042-2674

Yasuo Ohnishi − *Department of Biotechnology, Graduate School of Agricultural and Life Sciences, The University of Tokyo, Tokyo 113-8657, Japan; Collaborative Research Institute for Innovative Microbiology, The University of Tokyo, Tokyo 113-8657, Japan*

Complete contact information is available at: https://pubs.acs.org/10.1021/acsomega.4c05706

Notes

The authors declare no competing financial interest.

ACKNOWLEDGMENTS

This work was supported by the Japan Society for the Promotion of Science KAKENHI Grant Numbers JP19H05681 (S.S.) and JP19H05685 (Y.O.).

REFERENCES

(1) Silhavy, T. J.; Kahne, D.; Walker, S. The Bacterial Cell Envelope. *Cold Spring Harbor Perspect. Biol.* **2010**, *2*, a000414.

(2) Caforio, A.; Driessen, A. J. M. Archaeal Phospholipids: Structural Properties and Biosynthesis. *Biochim. Biophys. Acta, Mol. Cell Biol. Lipids* **2017**, *1862*, 1325−1339.

(3) van Wolferen, M.; Pulschen, A. A.; Baum, B.; Gribaldo, S.; Albers, S.-V. The Cell Biology of Archaea. *Nat. Microbiol.* **2022**, *7*, 1744−1755.

(4) Sleytr, U. B.; Schuster, B.; Egelseer, E.-M.; Pum, D. S-Layers: Principles and Applications. *FEMS Microbiol. Rev.* **2014**, *38*, 823−864.

(5) Rinke, C.; Schwientek, P.; Sczyrba, A.; Ivanova, N. N.; Anderson, I. J.; Cheng, J.-F.; Darling, A.; Malfatti, S.; Swan, B. K.; Gies, E. A.; et al. Insights into the Phylogeny and Coding Potential of Microbial Dark Matter. *Nature* **2013**, *499*, 431−437.

(6) Parenti, F.; Coronelli, C. Members of the Genus *Actinoplanes* and Their Antibiotics. *Annu. Rev. Microbiol.* **1979**, *33*, 389−411.

(7) Amore, R.; Hollenberg, C. P. Xylose Isomerase from *Adinoplanes missouriensis*: Primary Structure of the Gene and the Protein. *Nucleic Acids Res.* **1989**, *17*, 7515−7515.

(8) Simone, M.; Monciardini, P.; Gaspari, E.; Donadio, S.; Maffioli, S. I. Isolation and Characterization of NAI-802, a New Lantibiotic Produced by Two Different *Actinoplanes* Strains. *J. Antibiot.* **2013**, *66*, 73−78.

(9) Couch, J. N. Some New Genera and Species of the Actinoplanaceae. *J. Elisha Mitchell Sci. Soc.* **1963**, *79*, 53−70.

(10) Yamamura, H.; Ohnishi, Y.; Ishikawa, J.; Ichikawa, N.; Ikeda, H.; Sekine, M.; Harada, T.; Horinouchi, S.; Otoguro, M.; Tamura, T.; et al. Complete Genome Sequence of the Motile Actinomycete *Actinoplanes missouriensis* 431^{T} (= NBRC 102363^{T}). *Stand. Genomic Sci.* **2012**, *7* (7), 294−303.

(11) Mouri, Y.; Konishi, K.; Fujita, A.; Tezuka, T.; Ohnishi, Y. Regulation of Sporangium Formation by BldD in the Rare Actinomycete *Actinoplanes missouriensis*. *J. Bacteriol.* **2017**, *199*, No. e00840−16.

(12) Hashiguchi, Y.; Tezuka, T.; Mouri, Y.; Konishi, K.; Fujita, A.; Hirata, A.; Ohnishi, Y. Regulation of Sporangium Formation, Spore Dormancy, and Sporangium Dehiscence by a Hybrid Sensor Histidine Kinase in *Actinoplanes missouriensis*: Relationship with the Global Transcriptional Regulator TcrA. *J. Bacteriol.* **2020**, *202*, No. e00228−20.

(13) Tezuka, T.; Mitsuyama, K.; Date, R.; Ohnishi, Y. A Unique Sigma/Anti-Sigma System in the Actinomycete *Actinoplanes missouriensis*. *Nat. Commun.* **2023**, *14*, 8483.

(14) Tezuka, T.; Ohnishi, Y. Surface Structure and Nanomechanical Properties of *Actinoplanes missouriensis* Sporangia Analyzed Via Atomic Force Microscopy. *Biosci., Biotechnol., Biochem.* **2022**, *86*, 552−556.

(15) Hu, S.; Tahara, Y. O.; Tezuka, T.; Miyata, M.; Ohnishi, Y. Architecture of *Actinoplanes missouriensis* Sporangia and Zoospores Visualized Using Quick-Freeze Deep-Etch Electron Microscopy. *Biosci., Biotechnol., Biochem.* **2024**, *88*, 225−229.

(16) Krafft, C.; Schmitt, M.; Schie, I. W.; Cialla-May, D.; Matthäus, C.; Bocklitz, T.; Popp, J. Label-Free Molecular Imaging of Biological Cells and Tissues by Linear and Nonlinear Raman Spectroscopic Approaches. *Angew. Chem., Int. Ed.* **2017**, *56*, 4392−4430.

(17) Yue, S.; Slipchenko, M. N.; Cheng, J.-X. Multimodal Nonlinear Optical Microscopy. *Laser Photon. Rev.* **2011**, *5*, 496−512.

(18) Segawa, H.; Okuno, M.; Kano, H.; Leproux, P.; Couderc, V.; Hamaguchi, H. Label-Free Tetra-Modal Molecular Imaging of Living Cells with CARS, SHG, THG and TSFG (Coherent Anti-Stokes Raman Scattering, Second Harmonic Generation, Third Harmonic Generation and Third-Order Sum Frequency Generation). *Opt. Express* **2012**, *20*, 9551−9557.

(19) Cheng, J.-X.; Xie, X. S. Coherent Anti-Stokes Raman Scattering Microscopy: Instrumentation, Theory, and Applications. *J. Phys. Chem. B* **2004**, *108*, 827−840.

(20) Kano, H.; Maruyama, T.; Kano, J.; Oka, Y.; Kaneta, D.; Guerenne, T.; Leproux, P.; Couderc, V.; Noguchi, M. Ultra-Multiplex CARS Spectroscopic Imaging with 1-Millisecond Pixel Dwell Time. *OSA Continuum* **2019**, *2*, 1693−1705.

(21) Campagnola, P. J.; Clark, H. A.; Mohler, W. A.; Lewis, A.; Loew, L. M. Second harmonic imaging microscopy of living cells. *J. Biomed. Opt.* **2001**, *6*, 277−286.

(22) Cox, G. Biological Applications of Second Harmonic Imaging. *Biophys. Rev.* **2011**, *3*, 131−141.

(23) Campagnola, P. Second Harmonic Generation Imaging Microscopy: Applications to Diseases Diagnostics. *Anal. Chem.* **2011**, *83*, 3224−3231.

(24) Barad, Y.; Eisenberg, H.; Horowitz, M.; Silberberg, Y. Nonlinear Scanning Laser Microscopy by Third Harmonic Generation. *Appl. Phys. Lett.* **1997**, *70*, 922−924.

(25) Müller, M.; Squier, J.; Wilson, K. R.; Brakenhoff, G. J. 3D Microscopy of Transparent Objects Using Third-Harmonic Generation. *J. Microsc.* **1998**, *191*, 266−274.

(26) Weigelin, B.; Bakker, G.-J.; Friedl, P. Third Harmonic Generation Microscopy of Cells and Tissue Organization. *J. Cell Sci.* **2016**, *129*, 245−255.

(27) Tezuka, T.; Nakane, D.; Kimura, T.; Ohnishi, Y. Preparation of *Actinoplanes missouriensis* Zoospores and Assay for Their Adherence to Solid Surfaces. *Bio-Protoc.* **2019**, *9*, No. e3458.

(28) Matsuda, A.; Sakaguchi, N.; Shigeto, S. Can Cells Maintain Their Bioactivity in Ionic Liquids? A Novel Single-Cell Assessment by Raman Microspectroscopy. *J. Raman Spectrosc.* **2019**, *50*, 768−777.

(29) Kanno, N.; Kato, S.; Ohkuma, M.; Matsui, M.; Iwasaki, W.; Shigeto, S. Nondestructive Microbial Discrimination Using Single-Cell Raman Spectra and Random Forest Machine Learning Algorithm. *STAR Protoc.* **2022**, *3*, 101812.

(30) Sasaki, R.; Toda, S.; Sakamoto, T.; Sakuradani, E.; Shigeto, S. Simultaneous Imaging and Characterization of Polyunsaturated Fatty

Acids, Carotenoids, and Microcrystalline Guanine in Single *Aurantiochytrium limacinum* Cells with Linear and Nonlinear Raman Microspectroscopy. *J. Phys. Chem. B* **2023**, *127*, 2708−2718.
(31) Okuno, M.; Kano, H.; Leproux, P.; Couderc, V.; Hamaguchi, H. Ultrabroadband Multiplex CARS Microspectroscopy and Imaging Using a Subnanosecond Supercontinuum Light Source in the Deep near Infrared. *Opt. Lett.* **2008**, *33*, 923−925.
(32) Huang, C.-K.; Ando, M.; Hamaguchi, H.; Shigeto, S. Disentangling Dynamic Changes of Multiple Cellular Components During the Yeast Cell Cycle by *in Vivo* Multivariate Raman Imaging. *Anal. Chem.* **2012**, *84*, 5661−5668.
(33) Uzunbajakava, N.; Lenferink, A.; Kraan, Y.; Volokhina, E.; Vrensen, G.; Greve, J.; Otto, C. Nonresonant Confocal Raman Imaging of DNA and Protein Distribution in Apoptotic Cells. *Biophys. J.* **2003**, *84*, 3968−3981.
(34) Baek, S.-J.; Park, A.; Ahn, Y.-J.; Choo, J. Baseline Correction Using Asymmetrically Reweighted Penalized Least Squares Smoothing. *Analyst* **2015**, *140*, 250−257.
(35) Paatero, P.; Tapper, U. Positive Matrix Factorization: A Non-Negative Factor Model with Optimal Utilization of Error Estimates of Data Values. *Environmetrics* **1994**, *5*, 111−126.
(36) Lee, D. D.; Seung, H. S. Learning the Parts of Objects by Non-Negative Matrix Factorization. *Nature* **1999**, *401*, 788−791.
(37) Boutsidis, C.; Gallopoulos, E. SVD Based Initialization: A Head Start for Nonnegative Matrix Factorization. *Pattern Recognit.* **2008**, *41*, 1350−1362.
(38) Tibshirani, R. Regression Shrinkage and Selection Via the Lasso. *J. R. Statist. Soc. B* **1996**, *58*, 267−288.
(39) Rinia, H. A.; Bonn, M.; Müller, M.; Vartiainen, E. M. Quantitative CARS Spectroscopy Using the Maximum Entropy Method: The Main Lipid Phase Transition. *ChemPhysChem* **2007**, *8*, 279−287.
(40) Vartiainen, E. M.; Rinia, H. A.; Müller, M.; Bonn, M. Direct Extraction of Raman Line-Shapes from Congested CARS Spectra. *Opt. Express* **2006**, *14*, 3622−3630.
(41) Yasuda, M.; Takeshita, N.; Shigeto, S. Inhomogeneous Molecular Distributions and Cytochrome Types and Redox States in Fungal Cells Revealed by Raman Hyperspectral Imaging Using Multivariate Curve Resolution−Alternating Least Squares. *Anal. Chem.* **2019**, *91*, 12501−12508.
(42) Saito, S.; Tasumi, M. Normal-Coordinate Analysis of β-Carotene Isomers and Assignments of the Raman and Infrared Bands. *J. Raman Spectrosc.* **1983**, *14*, 310−321.
(43) Huang, C.-K.; Hamaguchi, H.; Shigeto, S. *In Vivo* Multimode Raman Imaging Reveals Concerted Molecular Composition and Distribution Changes During Yeast Cell Cycle. *Chem. Commun.* **2011**, *47*, 9423−9425.
(44) Parekh, S. H.; Lee, Y. J.; Aamer, K. A.; Cicerone, M. T. Label-Free Cellular Imaging by Broadband Coherent Anti-Stokes Raman Scattering Microscopy. *Biophys. J.* **2010**, *99*, 2695−2704.
(45) Miyazaki, S.; Leproux, P.; Couderc, V.; Hayashi, Y.; Kano, H. Multimodal Nonlinear Optical Imaging of *Caenorhabditis elegans* with Multiplex Coherent Anti-Stokes Raman Scattering, Third-Harmonic Generation, Second-Harmonic Generation, and Two-Photon Excitation Fluorescence. *Appl. Phys. Express* **2020**, *13*, 072002.
(46) Stoller, P.; Reiser, K. M.; Celliers, P. M.; Rubenchik, A. M. Polarization-Modulated Second Harmonic Generation in Collagen. *Biophys. J.* **2002**, *82*, 3330−3342.
(47) Carey, P. R. *Biochemical Applications of Raman and Resonance Raman Spectroscopies*; Academic Press: New York, 1982.
(48) Naumann, D. FT-Infrared and FT-Raman Spectroscopy in Biomedical Research. *Appl. Spectrosc. Rev.* **2001**, *36*, 239−298.
(49) De Gelder, J.; De Gussem, K.; Vandenabeele, P.; Moens, L. Reference Database of Raman Spectra of Biological Molecules. *J. Raman Spectrosc.* **2007**, *38*, 1133−1147.
(50) Czamara, K.; Majzner, K.; Pacia, M. Z.; Kochan, K.; Kaczor, A.; Baranska, M. Raman Spectroscopy of Lipids: A Review. *J. Raman Spectrosc.* **2015**, *46*, 4−20.
(51) Ding, T.; Yang, L.-J.; Zhang, W.-D.; Shen, Y.-H. The Secondary Metabolites of Rare Actinomycetes: Chemistry and Bioactivity. *RSC Adv.* **2019**, *9*, 21964−21988.

https://doi.org/10.1021/acsomega.4c05706
ACS Omega 2024, 9, 39956−39964